Article

Not peer-reviewed version

Primary Trace Humidity Standards and SI-Traceable Trace Water Measurements in Ultra-High Purity Process Gases

Vito Fernicola *, Giulio Beltramino, Antonio Castrillo, Rugiada Cuccaro, Regina Deschermeier, Volker Ebert, Diana Enescu, Livio Gianfrani, Philipp J. Gliese, Stefania Gravina, Domen Hudoklin, Rezvaneh Nobakht, Isidora Radičević, Lucia Rosso, Shahin Tabandeh

Posted Date: 30 April 2026

doi: 10.20944/preprints202604.2096.v1

Keywords: ultra-high purity gases; frost-point temperature; water vapour amount fraction; trace humidity standards; trace water measurement; spectroscopic analysers

 doi:10.20944/preprints202604.2096.v1

Article

Primary Trace Humidity Standards and SI-Traceable Trace Water Measurements in Ultra-High Purity Process Gases

Vito Fernicola [1,*], Giulio Beltramino [1], Antonio Castrillo [2], Rugiada Cuccaro [1], Regina Deschermeier [3], Volker Ebert [3], Diana Enescu [1,4], Livio Gianfrani [2], Philipp J. Gliese [3], Stefania Gravina [2], Domen Hudoklin [5], Rezvaneh Nobakht [1], Isidora Radičević [5], Lucia Rosso [1] and Shahin Tabandeh [6]

[1] INRIM Istituto Nazionale di Ricerca Metrologica, Italy
[2] Università degli Studi della Campania "Luigi Vanvitelli", Italy
[3] PTB Physikalisch-Technische Bundesanstalt, Germany
[4] Valahia University of Targoviste, Romania
[5] UL FE University of Ljubljana, Faculty of Electrical Engineering, Slovenia
[6] VTT Technical Research Centre of Finland Ltd., Centre for Metrology MIKES, Finland
* Correspondence: v.fernicola@inrim.it

Abstract

Trace water is one of the most critical matrix contaminants in ultra-high purity (UHP) process gases, like argon (Ar) and nitrogen (N_2), and many others. Even trace amounts can severely degrade the quality of many products reliant on these gases. Despite its importance to advanced technology sectors, notably semiconductor manufacturing, it has proven quite difficult to realize preparative or analytical trace water metrology over the full amount fraction range needed or in the broad spectrum of industrially relevant matrix gases. Within the EU-funded PROMETH2O project consortium, this challenge has been addressed through the development or significant improvement of traceable measurement methods and standards spanning 5 nmol mol^{-1} to 5 µmol mol^{-1}, tailored for use in UHP process gas production, such as Ar, N2 and hydrogen (H2). The measurement ranges were extended and the uncertainties were improved, while being consistent with current best practice at primary humidity standards laboratories. These capabilities were validated in applications relevant to process instrumentation and the gas industry. A distributed metrological infrastructure at various European National Metrology Institutes and partner sites now provides SI-traceable trace water measurements in various UHP, strongly supporting and extending the calibration capabilities for the gas and semiconductor industries and the associated stakeholders.

Keywords: ultra-high purity gases; frost-point temperature; water vapour amount fraction; trace humidity standards; trace water measurement; spectroscopic analysers

1. Introduction

Humidity, defined as the amount of water vapour present in gases, exerts a major influence on various chemical, physical, and biological processes. Accurate humidity control is crucial across numerous industries and technologies, as moisture levels significantly impact production costs, product quality and performance, safety standards, human health, and working environment conditions. Depending on application, gas purity requirements range from high-purity gases - typically exceeding 99.999% purity (grade 5.0), with total impurity amount fraction below 10 µmol·mol^{-1} - to ultra-high purity (UHP) gases exceeding 99.9999% purity (grade 6.0 or higher), with total impurity amount fraction in the nmol·mol^{-1} (ppb) or sub-ppb range. Various high-technology sectors utilize UHP bulk and speciality gases. Bulk gases (e.g., N_2, O_2, He, Ar, and H_2) are primarily

 doi:10.20944/preprints202604.2096.v1

used for blanketing, purging, and maintaining ultra-clean environments. Specialty gases (e.g., ammonia (NH_3) or hydrogen chloride (HCl)) are chemically reactive and utilized in smaller quantities for specific manufacturing processes, such as film deposition or doping.

UHP gases must maintain extremely low contaminant levels to prevent product or process degradation or contamination-related issues [1]. In this context, impurities denote any chemical substances present in trace amounts other than the principal gas component, whereas a contaminant is specifically defined as an undesired substance that negatively affects the target process or a process-related measurement. Therefore, while all contaminants are impurities, not all impurities are harmful contaminants. Among all potential contaminants in UHP gases, water vapour is considered one of the most critical due to its strong polarity and its tendency to adsorb onto metallic surfaces or into porous matrices [1]. Adsorption, in this context, refers to the accumulation of water vapour as a surface layer on a given material; the complementary process, desorption, releases bound molecules back into the gas phase and is equally significant for metrological applications at the ppb level.

Water vapour can persist within gas distribution systems - such as stainless steel pipelines, valves, and pressure regulators—even after extensive purging with dry inert gases like N_2 and Ar. More elevated water vapour levels can induce corrosion in gas delivery lines and adversely affect processing equipment, particularly when present in reactive gas mixtures such as hydrogen bromide (HBr) or anhydrous hydrogen chloride (HCl). In such environments, water vapour may react to form highly corrosive acidic surface layers that are prone to damage both gas lines and process equipment [1].

Trace humidity in gases is conventionally specified as a water vapour amount fraction (x_w) not exceeding 1 μmol·mol^{-1} (1 ppm), corresponding to a frost-point temperature below −75 °C. This threshold is consistent with the purity requirements specified in ISO 14687 for hydrogen fuel quality and with SEMI C3 for electronic specialty gases. For frost-point temperature measurements within the trace humidity range, various types of hygrometers are employed, including chilled-mirror hygrometers or laser spectroscopic gas analysers. Less expensive coulometric or metal-oxide sensors are also available.

This paper presents recent advances in trace water generation and measurement in UHP process gases. It focuses on the metrological traceability and the realisation of primary and reference humidity standards operating in the range from micromole per mole (ppm) to nanomole per mole (ppb). The paper is organised as follows. Section 2 presents trace water measurement techniques. Section 3 describes the primary and reference humidity standards developed within the PROMETH2O project, including saturation-based generators from three European NMIs and a coulometric generator. The description of a comb-locked cavity ring-down spectrometer is also reported. Section 4 presents the validation results and uncertainty budgets for such primary systems. Section 5 discusses the results and identifies future directions.

2. Measurement Techniques for Trace Water in UHP Gases

Accurate measurement of water vapour amount fractions in gases, particularly in the ppm to ppb range, presents a significant analytical challenge. Reactive and corrosive gas matrices exacerbate this challenge by reducing sensor stability and sensitivity, slow response times, high measurement drift, hysteresis, and, in severe cases, instrument failure e.g., by corrosion [2,3]. No single analytical technique universally satisfies all application requirements; each method presents a special combination among sensitivity, complexity, cost, robustness and response time [1,4]. Trace humidity may be quantified by a range of analytical methods, including gas chromatography (GC), mass spectrometry (MS), optical spectroscopy, and sensor-based techniques classified by sensing material and measured quantity; furthermore, sensors are often calibrated with respect to dew- or frost-point temperature even when the measurement principles and the measured quantity are different. The following subsections focus on the methods most relevant to UHP gas applications: chilled-mirror hygrometry and optical spectroscopy.

 doi:10.20944/preprints202604.2096.v1

2.1. Chilled-Mirror Dew/Frost-Point Hygrometry

Chilled-mirror dew/frost-point hygrometers (CMHs) are the primary reference instruments, measuring directly the thermodynamic quantity - corresponding to the thermodynamic equilibrium between gas-phase water vapour and the condensed phase. This thermodynamic measurand confers direct SI-traceability via the temperature scale. CMH instruments are consequently employed by National Metrology Institutes (NMIs) as transfer standards for humidity calibrations. They operate by cooling a polished metal mirror coated with a gold or rhodium coating by using a Peltier-based thermoelectric cooler (TEC) until condensation occurs. An integrated optical system detects the condensation via a reduction in reflected light intensity, while an embedded platinum resistance thermometer (PRT) records the mirror temperature. CMHs operate over approximately −110 °C to 95 °C dew/frost-point temperature, corresponding to water vapour amount fraction range from 10 nmol·mol^{-1} to approximately 0.85 mol·mol^{-1}, often with uncertainties below 0.1 °C [5,6]. Measurement uncertainty can be worsened by co-condensation of contaminant species as well as by Raoult or Kelvin effects from soluble or insoluble mirror deposits [7]. PRT self-heating and an inherently slow response time, particularly at low humidities, limit their suitability in industrial applications [8,9].

2.2. Optical Absorption Spectroscopy Methods

Optical absorption methods, such as the Fourier transform infrared (FTIR) spectroscopy enable simultaneous identification and quantification of multiple gas-phase species, including water vapour, down to low ppb levels [10]. Good selectivity for water vapour is achieved at spectral resolutions between 2 cm^{-1} and 4 cm^{-1} while sensitivity and detection limits can be scaled with absorption path length from a few millimetres to a few hundred metres. Detection limits between 10 ppb and 30 ppb are commonly achieved [11]. Below 10 ppb in reactive matrices, laser-based techniques are preferred owing to their higher selectivity and better sensitivity [4].

Tuneable diode laser absorption spectroscopy (TDLAS) provides highly selective and sensitive species measurements through targeted high-resolution molecular roto-vibrational absorption lines. The narrow laser linewidth confers greater selectivity when compared to FTIR, and the technique is amenable to fibre-optic integration [12–14]. Water vapour detection limits in the ppb range have been demonstrated in inert gases. TDLAS has also been successfully deployed across reactive and corrosive matrices [4,15,16]. In the semiconductor industry, where moisture in UHP bulk gases must remain below 10 ppb to prevent fabrication defects, TDLAS has been widely adopted as a complement to electrochemical sensors, which are susceptible to drift and ageing [16].

A first-principles variant of TDLAS, known as dTDLAS, is highly relevant for metrological hygrometry as it allows absolute, traceable water vapour detection without the need for instrument calibration. The calibration-free property was validated via comparison against the PTB humidity standard [17,18] and later validated between 10 µmol mol^{-1} and 350 µmol mol^{-1} via comparison with PTB coulometric trace water generator [40]. The dTDLAS analysers showed a relative standard uncertainty of 1.2 % and a precision of 23 nmol mol^{-1} at 2-s time resolution.

Among optical methods, laser-based cavity ring-down spectroscopy (CRDS) is one with the highest sensitivity capable of quantifying trace gases at ppb or sub-ppb (ppt) levels by measuring the decay time of a light pulse within a high-finesse optical cavity [19–22]. The cavity enhancement enables effective path lengths up to tens of kilometres, that is not achievable even by multi-reflection FTIR and TDLAS cells. For this reason, CRDS was the spectroscopic method of choice within PROMETH2O; the comb-locked CRDS system developed at the University of Campania ‘Luigi Vanvitelli’ for SI-traceable trace water detection in UHP gases is described in Section 3.3.

3. Realisation of Primary Trace Humidity Standards

The demand for traceable trace humidity measurements has prompted NMIs to develop primary generators and associated metrological infrastructure to underpin the calibration of trace moisture sensors and analysers in UHP gas applications.

 doi:10.20944/preprints202604.2096.v1

This section describes the primary humidity generators developed within PROMETH2O and a primary measurement method based on CRDS. Three thermodynamic generators based on ice saturation and one coulometric generator collectively cover water vapour amount fractions from a few nanomoles per mole to several micromoles per mole in N_2, CDA, and Ar matrices. These systems encompass multiple traceability approaches, including thermodynamic saturation, electrochemical, and gravimetric principles. Among the saturation-based methods, two primary thermodynamic configurations are predominantly used to generate traceable reference gas mixtures.

3.1. Saturation-Based Humidity Generators

- Single-temperature, single-pressure (1T-1P) principle. In a 1T-1P system, a carrier gas is fully saturated with water vapour at a controlled thermodynamic state, defined by a constant saturation temperature (T_s) and pressure (p_s) typically near atmospheric pressure. Following saturation, the gas stream is directly delivered to the devices under calibration. If the pressure drop between the saturator and the point of use is negligible, then $T_s \cong T_{fp}$.
- Single-temperature, two-pressure (1T-2P) principle. In a 1T-2P system, a carrier gas is fully saturated with water vapour at a rigorously controlled thermodynamic state, defined by a constant saturation temperature and pressure (p_s). Following saturation, the gas stream undergoes an isothermal expansion to a lower pressure (p_c), typically near atmospheric conditions. Because the amount fraction of water vapour is conserved during expansion, the output frost-point temperature is a function of the pressure ratio and the saturation vapour pressure.

Table 1 summarises the main performance characteristics and technical capabilities of the humidity generators developed and validated by various metrological institutes during the project PROMETH2O. The table presents technical details including working principles, carrier, gases, operating ranges, and associated measurement uncertainties.

Table 1. Summary of Primary Humidity Generators for Trace Water Measurement in Pure Gases.

No.	Generator type	Working Principle	Carrier Gases	Operating Range	Measurement uncertainty
1	Saturation-based (INRIM 03 Mk2)	Saturation (1T-2P)	N_2, CDA, Ar	-105 °C to 0 °C, 0.7 MPa	0.04 K to 0.14 K
2	Saturation-based (UL FE)	Saturation (1T-2P)	N_2, CDA, Ar	-95 °C to +20 °C, 2 MPa	0.04 K to 0.13 K
3	Saturation-based (VTT)	Saturation (1T-2P)	N_2, CDA, Ar	-100 °C to 0 °C, 0.7 MPa	0.04 K to 0.12 K
4	Coulometric (CTHG)	Electrolysis + stream mixing	N_2	5 nmol/mol – 0.04 mol/mol	depending on the range and measurand

3.1.1. INRIM Primary Trace Humidity Generator (1T-2P)

The trace humidity generator developed at INRiM, referred to as INRIM 03 Mark 2, operates in a single-temperature two-pressure (1T-2P) mode. In this configuration the carrier gas, such as N_2 or Ar, is first saturated at the temperature T_s and pressure p_s higher than the atmospheric pressure and then expanded to the point-of-use pressure p_c slightly higher than the atmospheric pressure (≈ 1150 hPa). By expanding the humid carrier gas from a saturator pressure as high as 6500 hPa, a frost-point temperature as low as −105 °C is achievable (or, equivalently, a water vapour amount fraction down to 4 nmol·mol^{-1}) at the generator outlet, thereby overcoming the frost-point temperature downward limit of the previous version [29]. Under the assumption of mass conservation, the water vapour amount fraction does not change during the expansion; thus, the frost-point temperature of the humid gas T_{fp} at the outlet of the generator can be determined using the following relation:

$$\frac{f(p_s, T_s) \cdot e_s(T_s)}{p_s} = \frac{f(p_c, T_{fp}) \cdot e_s(T_{fp})}{p_c} \quad (1)$$

 doi:10.20944/preprints202604.2096.v1

where the left-hand member of the equation is the amount fraction of water vapour, xw, calculated from the known variables p_s and T_s, p_c is the point-of-use pressure after the expansion, $f(p_c,T_{fp})$ is the enhancement factor at T_{fp} and p_c while $e_s(T_{fp})$ is the saturation water vapour pressure of its pure phase at T_{fp}. Both enhancement factors were evaluated using the formulation provided by Greenspan [30]. By solving Eq. (1) for $e_s(T_{fp})$ and then applying Hardy's formulation [31], the frost-point temperature can be calculated [31].

The experimental setup of the humidity generator is shown in Figure 1.

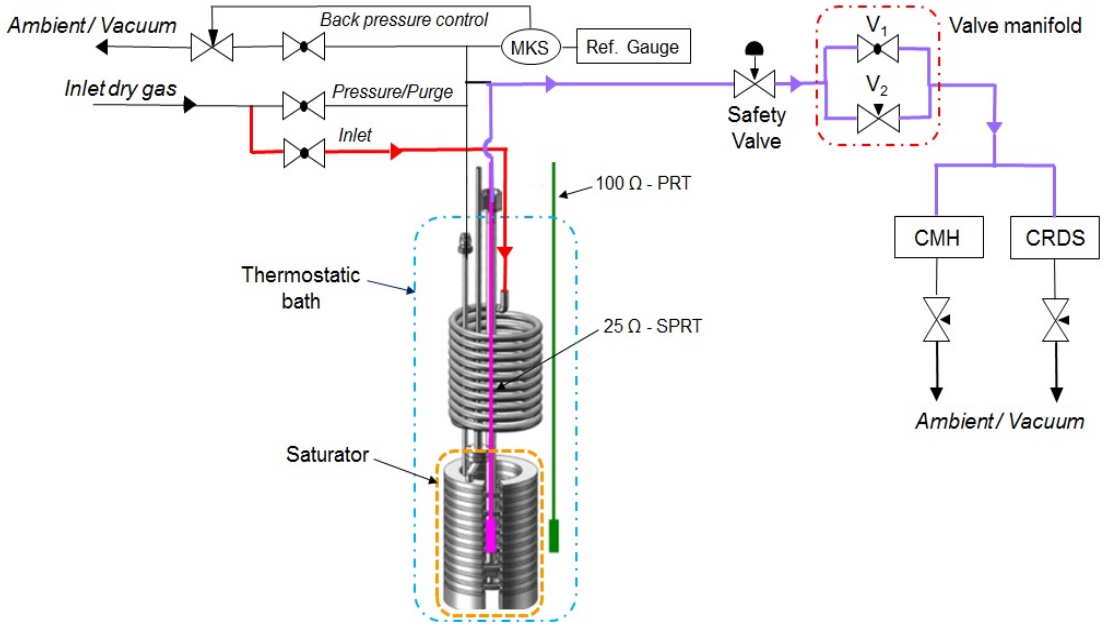

Figure 1. Schematic of the INRIM 03 Mark 2 humidity generator experimental setup.

The core of the humidity generator consists of an isothermal saturator partially filled with ice, hosted in a thermostatic bath, whose temperature T_b is measured by a 100 Ω platinum resistance thermometer (PRT) immersed into the liquid bath at a depth corresponding to the saturator outlet. A 25 Ω standard platinum resistance thermometer (SPRT) is inserted into the outlet tube of the saturator to accurately determine the saturation temperature T_s of the humid gas. The saturation pressure p_s is controlled by a PID-based back-pressure regulator and it is measured by means of a high-accuracy capacitance manometer (Paroscientific 745 – 0.7 MPa f.s.). The dry gas flow rate $\dot{V}$ is controlled and measured at the inlet of the saturator in the range from 2 L·min^{-1} to 6 L·min^{-1}. A valve manifold at the saturator's outlet enables the generator to operate in either the 1T-1P (by a high-flow diaphragm bypass valve) or 1T-2P mode (by a bellows sealed metering valve). The point-of-use pressure, p_c, is measured by a high-accuracy barometer (Keller PAA-33X – 1200 hPa f.s.).

The humid gas flow at the outlet of the generator is split into two lines, to simultaneously feed different types of hygrometers or analysers. Check instruments currently in use include:

i. a chilled-mirror hygrometer (PI/MBW mod. SLX) for low frost-point temperature measurements from -110 °C to +20 °C;
ii. a cavity ring-down spectrometer (Photonics Technology mod. Pure^{n}-T H_2O) for water vapour amount fraction measurements between 0.2 nmol·mol^{-1} and 5 µmol·mol^{-1}.

3.1.2. UL FE Primary Trace Humidity Generator (1T-2P)

The system operates as a single-pass humidity generator, wherein dry, filtered carrier gas (air, N_2, or Ar of 5-N purity or better) flows through the apparatus a single time prior to being exhausted [32]. As illustrated in Figure 2, the architecture comprises a filter, a mass-flow controller (MFC), and a temperature-controlled liquid bath that houses both the heat exchanger and the saturator.

 doi:10.20944/preprints202604.2096.v1

Following supplementary purification, the gas flow rate is established by the MFC and directed through the heat exchanger into the saturator (with valves V3 and V4 open, and valve V2 closed). The internal saturation path spans approximately 3 m to ensure complete thermodynamic saturation in a single pass [33]. The conditioned gas subsequently exits toward the hygrometer undergoing calibration (via valves V5 and/or V6). During cooling and drying phases, a reverse-flow operation (utilizing open valves V2, V4, and V7) is employed to prevent water adsorption on the outlet tubing, which would otherwise systematically increase the generated moisture content.

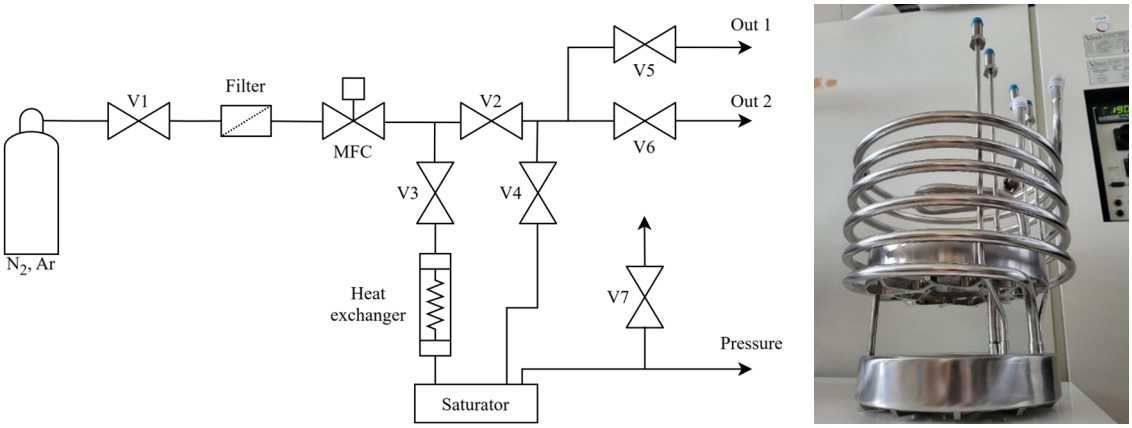

Figure 2. Schematic diagram of the UL FE ultra-low frost point generator and the stainless-steel high-pressure saturator.

The generator supports both single-pressure and two-pressure operational modes. In single-pressure mode, the saturator and the sensor are maintained at nearly equal pressures, exhibiting only a nominal pressure drop [34]. For two-pressure operation, the gas is initially saturated at an elevated pressure and subsequently expanded isothermally to a lower pressure via an expansion valve located downstream of the saturator. This thermodynamic expansion extends the achievable low frost-point range to temperatures below −100 °C. The core component of the system is the stainless-steel saturator (Figure 2). Its minimum operating temperature is −95 °C, and it has been pressure-tested up to 2 MPa. The saturator must achieve full thermal and phase equilibration of the gas, compensating for the dew-point differential between the inlet and the outlet at flow rates sufficient to supply at least one hygrometer. The 3-m internal fluidic path guarantees efficient saturation [35]. To ensure thermal equilibrium, both the saturator and the heat exchanger are fully immersed in a temperature-stabilized liquid bath [36,37]. The bath temperature is monitored with high accuracy using a SPRT.

3.1.3. VTT Primary Trace Humidity Generator (1T-2P)

The VTT Low Frost Point Humidity Generator (LFPHG) is a thermodynamic saturation- and condensation-based primary humidity generator designed to operate in both single-temperature/single-pressure (1T–1P) and single-temperature/two-pressure (1T-2P) modes [38,39]. This system extends traceable humidity generation down to frost-point temperatures of -100 °C and accommodates operational pressures up to 0.7 MPa.

The VTT generator operates on the 1T-2P thermodynamic saturation principle as described in Section 3.1.1. Carrier gas is saturated at elevated pressure p_s and temperature T_s, then expanded isothermally to point-of-use pressure pc; the output frost-point temperature and water vapour amount fraction are determined by Eq. (1). The reference measurand, expressed as either T_{fp} or x_w, is determined by T_s, p_s, and p_c through Eq. (1), and SI traceability is established through calibrated temperature and pressure measurements combined with this validated thermodynamic model.

The architecture of the generator (depicted in Figure 3) comprises the following key components: a thermostatically controlled ice saturator/condenser fully immersed in a thermally characterized liquid bath; a calibrated SPRT dedicated to accurate saturation temperature measurement; a back-

 doi:10.20944/preprints202604.2096.v1

pressure controller that facilitates system operation at pressures up to 0.7 MPa; a gas purification stage employing a getter dryer to establish a stable base-level humidity; a two-flow conditioning and mixing stage; dedicated outlet branches designed for the connection and calibration of the device under calibration (DUC).

To minimize the effects of incomplete saturation, the saturator design incorporates an extended evaporation path to guarantee thermodynamic equilibrium. Furthermore, thermal stability and spatial temperature homogeneity are continuously monitored using calibrated resistance thermometers. The operational gas pressures at both the saturation stage and the generator outlet are measured using traceably calibrated pressure transducers.

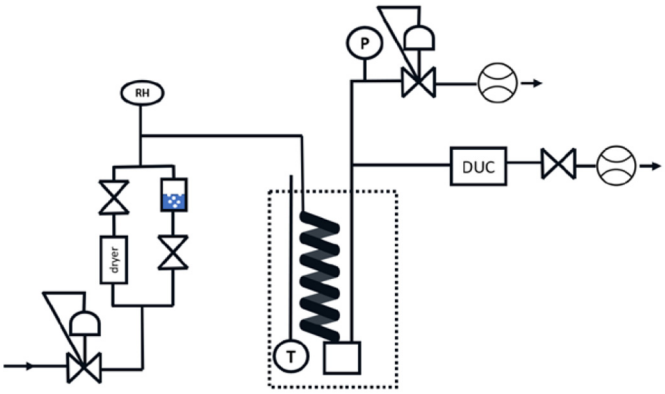

Figure 3. Schematic of the VTT two-pressure low-temperature frost-point generator, where RH denotes a capacitive hygrometer measuring in RH unit, T represents the SPRT, P indicates the pressure gauge, and DUC is the device under calibration.

3.2. PTB Coulometric Primary Standard

A coulometric trace-humidity generator typically consists of four main components: an electrolyser (a), a cooling trap (b), a catalyst acting as the humidification unit (c), and a mixing setup (d). This architecture is illustrated in Figure 4, which depicts the inert-gas coulometric trace-humidity generator (CTHG) developed at PTB [40,41].

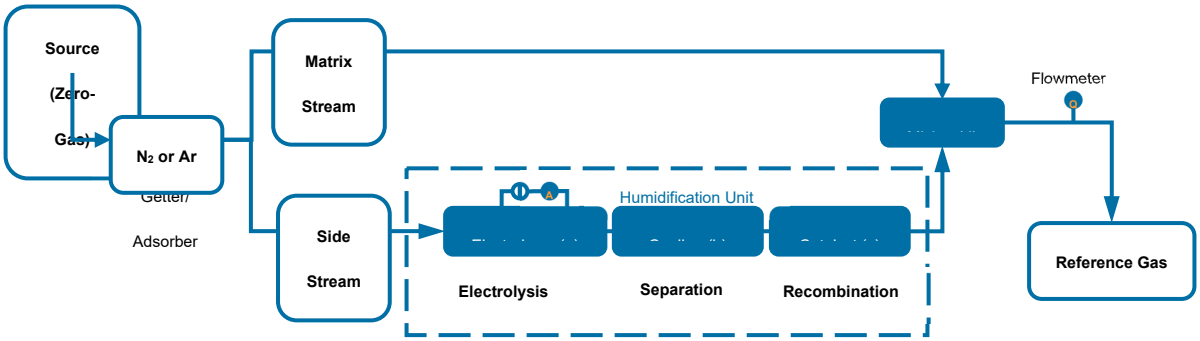

Figure 4. Schematic of the PTB Coulometric Trace Humidity Generator.

The core of the humidification unit is formed by modules (a) and (c). The cooling trap is utilized to condense and remove excess water vapour originating from the electrolysis procedure, which can occur due to saturation when an aqueous electrolyte is employed. The mixing setup enables the generator to operate across a broad water vapour amount fraction range, from 5 nmol mol^{-1} up to 0.04

 doi:10.20944/preprints202604.2096.v1

mol mol^{-1}, corresponding to a frost-point temperature range of approximately −100 °C up to −30 °C at ambient pressure.

CTHG operates on the principle of electrochemical hydrolysis according to Faraday's law, followed by consecutive catalytic recombination to form water. This process encompasses two fundamental steps:

(1) Hydrolysis: $2\,H_2O_{(l)} \rightarrow 2H_{2\,(g)} + O_{2\,(g)}$

(2) Catalytic Recombination: $2H_{2\,(g)} + O_{2\,(g)} \rightarrow 2\,H_2O_{(g)}$

For an ideal reaction, it is assumed that the amount of water molecules, n, is correlated as follows:

$$n_{\text{water,hydrolized (1)}} = n_{H_{2(g)}} = n_{\text{water,converted (2)}} \tag{2}$$

The amount of hydrolysed water molecules correlates with the number of transferred electrons, and consequently, the electric charge (Q). The subsequent recombination reaction (2) is kinetically controlled and quantitative, ensuring the full conversion of the evolved gases back into water vapour. Consequently, the generated humidity is directly traceable to electrical current. The correlation between the current and the resulting mole fraction is given by:

$$Q = I \cdot t = F \cdot z \cdot n_{\text{water,converted (2)}} \leftrightarrow n_{\text{water,converted (2)}} = \frac{I \cdot t}{F \cdot z} \tag{3}$$

where

F = Faraday constant, z = number of transferred electrons, t = time, Q = electric charge, I = electric current.

The humidification unit is embedded within a mixing setup. Inert gases, such as N2 are utilized as the source gas. The inert gas serves as a carrier, ensuring safe generator operation while enabling the generation of low water amount fractions in the reference gas via precise dilution. Regarding operational safety, hydrogen exhibits a lower explosive limit of 4 % and an upper limit of 77 % [42]. To guarantee safe operation, the evolved H_2 and O_2 gases must be adequately diluted. Furthermore, the mixing setup is highly beneficial for reaching the lowest trace-humidity range. The mixing ratio r is given by Eq. (4) [40]:

$$r = \frac{m_w}{m_{N_2}} = \frac{M_w}{M_{N_2}} \frac{V_0}{\dot{V}} \frac{I}{z \cdot F} \tag{4}$$

where

m_V= mass of water, m_{N_2}= mass of nitrogen, M_V= molar mass of water, M_{N_2}= molar mass of nitrogen, V_0= molar volume of ideal gas, $\dot{V}$= flow rate of reference gas at 0 °C and 1013.25 hPa.

Eq. (5) calculates the amount fraction of water vapour x_w obtained from the mixing ratio as follows:

$$x_w = \frac{r}{\frac{M_w}{M_{N_2}} + r} + x_{\text{blank}} \tag{5}$$

Generators operating on these coulometric principles are cumulative by nature, meaning they add water but cannot actively remove existing humidity from the gas stream. Therefore, the inherent water content of the source gas (x_{blank} e.g., N_2) must be known and maintained below a specific threshold dictated by the target water vapour amount fraction and the desired measurement uncertainty level. This baseline water content is actively accounted for in the final calculation of x_w.

Since coulometric trace water generators are not based on thermodynamic equilibrium, they provide a complementing technique to validate and compare to other generator types like saturation-based generators. At PTB, this type of generator is used to reach very low amount fractions due to the flexibility and dynamic approach of this system. However, it should be noted that the electrode reactions are sensitive to pressure, temperature, and available reactive surface sites. Stable generator operation, particularly at low frost-point temperatures, therefore, requires stable gas flow and

 doi:10.20944/preprints202604.2096.v1

pressure isolation from environmental fluctuations [41]. Thorough characterisation of all three modules is required to model generator behaviour accurately. Deviations from the ideal reactions are accounted for by applying module-specific efficiency factors determined in preliminary experiments; the associated uncertainty contributions are propagated to the combined measurement uncertainty budget [41].

At the time of writing, experimental validation of the PTB coulometric generator is in progress. Preliminary comparisons with traceable CMH indicate agreement within the combined expanded uncertainty; a full uncertainty characterisation and inter-laboratory validation will be reported in a dedicated publication upon completion of the programme.

3.3. Comb-Locked Cavity Ring-Down Spectrometer (University of Campania)

The principle of operation of CRDS relies on the observation of the temporal evolution of the light coupled in a high-finesse optical cavity. When the injected laser radiation is suddenly turned off, the intracavity field decays exponentially, and the rate of this decay carries direct information about the total optical losses inside the cavity. In an idealized situation, where mirror transmission dominates over other losses, the decay time, τ, is determined by the reflectivity of the mirrors and the length of the cavity. When an absorbing molecular species is present inside the cavity, optical losses increase and the decay time becomes shorter and frequency dependent. By comparing the decay constant at a given laser frequency with the empty-cavity decay constant, τ_0, the absorption coefficient, α, at frequency ν is related to the ring-down times by the equation:

$$\alpha(\nu) = \frac{1}{c}\left(\frac{1}{\tau(\nu)} - \frac{1}{\tau_0}\right) \tag{6}$$

where c is the vacuum speed of light, and ν is the laser frequency. Since it is directly proportional to the number density of the absorbing molecules, CRDS is inherently suited to absolute determinations of trace-gas concentrations. Over the last decades, several implementations of CRDS have been proposed, their common focus being the achievement of remarkable sensitivities, which often have been pushed up to the part-per-trillion (ppt) level [23].

In the case of trace water detection in high-purity gases, the water mole fraction, x_w, can be determined by using the following expression:

$$x_{\mathrm{w}} = \frac{\alpha_{\mathrm{TOT}} \cdot k_{\mathrm{B}} \cdot T}{S(T) \cdot p} \tag{7}$$

where α_{TOT} is the integrated absorption coefficient, k_{B} is the Boltzmann constant, T is the thermodynamic temperature, $S(T)$ is the temperature-dependent line intensity, and p is the gas pressure.

The uncertainty of the retrieved molecular concentration critically depends on the determination of the integrated absorption coefficient. The latter, in turn, passes through two important requirements: an absolute and highly-reproducible frequency scale underneath the absorption spectra, and the adoption of a refined line-shape model capable of capturing broadening and narrowing signatures of molecular spectra, such as the Doppler and collisional broadening, Dicke narrowing, speed-dependent effects, and possible asymmetries in the absorption profile.

The retrieval of x_{w} also requires accurate knowledge of the line intensity factor of the selected transition, whose value is usually provided from ab-initio calculations. For water transitions in the near-infrared, $S(T)$ is known with relative standard uncertainties of (0.1 to 1) % for well-characterised lines [24]; specific values used here are taken from the HITRAN2020 database.

The integration of an optical frequency comb synthesiser (OFCS) into a CRDS setup enables both absolute frequency determination and long-term spectral stability. In fact, the OFCS provides a grid of equally spaced, phase-coherent optical modes whose frequencies are known with high accuracy once its repetition rate and carrier-envelope offset frequencies are locked to a stable reference. By locking the probe laser to the comb and performing frequency scans through controlled offsets-locking schemes, the full absorption spectrum acquires an absolute, SI-traceable frequency axis,

 doi:10.20944/preprints202604.2096.v1

satisfying the principal requirement for absolute determinations of molecular number density. This capability also permits comparisons between spectra acquired at intervals of hours to days and, critically, multi-hour spectral averaging to suppress low-frequency noise from thermal and mechanical sources. This averaging is central to achieving record-level sensitivity [25,26].

The experimental platform, developed at the Ultrasensitive Molecular Spectroscopy Laboratory of the University of Campania, is shown schematically in Figure 5. It is based on the use of two tuneable external-cavity diode lasers operating near 1.39 μm, where well-isolated water rotational-vibrational transitions provide suitable absorption features [27,28]. In detail, one laser acts as a reference oscillator, hereafter referred to as RL, being stabilized to a COMB-locked high-finesse optical cavity by means of the Pound–Drever–Hall (PDH) locking technique. This technique reduces the RL linewidth to a few kHz for an observation time of 1 ms. The PDH cavity is locked against one of the teeth of the OFCS (MENLO Systems, FC1500-250-WG) with an offset frequency of 20 MHz. The optical frequency comb provides the absolute frequency scale, being disciplined by a GPS-stabilized Rb-clock which gives the time-base for the repetition rate (250 MHz) and the carrier-envelope offset frequencies (20 MHz). Under these conditions, the RL frequency can be absolutely determined by using the following equation:

$$\nu_{\mathrm{RL}} = N \cdot \nu_{\mathrm{REP}} + \nu_{\mathrm{CEO}} + \nu_{\mathrm{OFF}} \tag{8}$$

being *N* the comb tooth order. In this way, the RL becomes an intermediate optical link between the COMB and the laser interacting with the gaseous sample.

The second laser, designated as the probe laser (PL), is divided into two parts. One portion is employed to generate a beat note with the RL, as detected by a fibre-coupled high-bandwidth InGaAs photodiode, and used to phase-lock the PL to the RL, with a variable frequency offset provided by an RF-synthesizer operating at a frequency . This configuration allows the PL to be swept across the selected water absorption line by means of a fine tuning of , while the spectral purity of the PL is preserved to be the same as the reference laser.

The resulting system exhibits relative frequency stability at the level of 10^{-14} over one second of integration time, ensuring that the cumulative uncertainty of the laser frequency remains negligible compared to the intrinsic linewidth of the probed transition during long averaging windows [25].

The remaining portion of the PL beam, after passing into an acousto-optic modulator (AOM) and a booster-optical-amplifier (BOA), is down frequency shifted by 40 MHz and then directed to interact with the gas sample placed inside a hemispherical high-finesse optical resonator equipped with two mirrors having reflectivity exceeding 99.999 %. The empty-cavity decay time is about 285 μs [23], corresponding to an effective absorption path length approaching 170 km. The cavity is a 316-L stainless steel spacer with electropolished inner surfaces and is equipped with a precision pressure gauge and a platinum-resistance thermometer, ensuring that the pressure and temperature of the gas within the resonator are known with a relative accuracy better than 0.05 %. Constant gas flow conditions are maintained in the cavity via a pressure-forward controller to minimise adsorption and desorption effects.

Ring-down events are initiated by suddenly turning off the PL, sending a properly generated TTL signal to the AOM as well as to the BOA. The transmitted signal is detected by means of a low-noise InGaAs photodiode whose noise performance is well matched to the dynamic range of the decay process. A 16-bit digitizer records each decay with sampling parameters optimized to avoid aliasing effects while preserving temporal resolution. The entire system is controlled by a LabVIEW code which handles the frequency tuning of the RF-synthesizer, the digitizer, and performs synchronized data acquisitions.

Finally, the absolute frequency scale underneath the absorption spectra can be reconstructed by using the equation:

$$\nu_{\mathrm{PL}} = \nu_{\mathrm{RL}} + \nu_{\mathrm{RF}} \pm \nu_{\mathrm{AOM}} = N \cdot \nu_{\mathrm{REP}} + \nu_{\mathrm{CEO}} + \nu_{\mathrm{OFF}} + \nu_{\mathrm{RF}} \pm \nu_{\mathrm{AOM}} \tag{9}$$

 doi:10.20944/preprints202604.2096.v1

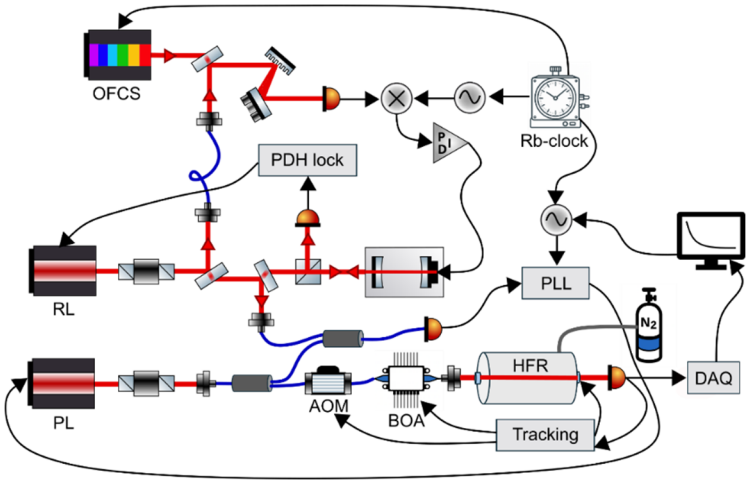

Figure 5. Sketch of the experimental set-up. OFCS stands for Rb-clock disciplined optical frequency comb synthesizer; RL, reference laser; PL, probe laser; PDH lock, Pound-Drever-Hall locking electronics; PID, proportional-integral-derivative controller; PLL, phase-locked loop; AOM, 40 MHz fiber-coupled acousto-optic modulator; BOA, booster optical amplifier; HFR, high-finesse optical resonator; Tracking, tracking electronics for the HFR; DAQ, data acquisition board.

To illustrate spectrometer performance, a broadband scan spanning approximately 9 GHz was recorded to simultaneously resolve four absorption features from the most abundant water isotopologues. The resulting spectrum, shown in Figure 6, resolves four absorption features corresponding to the following transitions [24]: the H17OH 11,1→11,0 component of the ν1+ν3 band at 7241.77470 cm^{-1}, the $H^{16}OD$ 22,0→22,1 component of the 2ν3 band at 7241.835537 cm^{-1}, the $H^{18}OH$ 94,5→95,4 component of the 2ν1 band at 7241.894981 cm^{-1}, and the $H^{16}OH$ 60,6→53,3 component of the 2ν1 band at 7241.951981 cm-1 [7]

The spectrum results from the average of 100 consecutive acquisitions; for each acquisition, every spectral point comes out from the average of 20 ring-down events. A single spectrum is acquired in about 140 s, with several spectral points and a frequency step of 80 MHz. The measurements were carried out using laboratory air continuously flowing through the measurement cell, at a constant pressure of 3.253(1) Torr, while the gas temperature was 23.95(3) °C.

The absorption profile was fitted using a sum of Voigt functions sharing common Doppler widths (properly rescaled by the ratios of the line centre frequencies and square root of the mass ratio). The resulting model well reproduces the experimental spectrum and permits identification of the isotopic contributions. For quantitative xw retrievals, at the operation pressures, the use of a Voigt line shape model may lead to a systematic uncertainty that is at the percent level. If sub-percent accuracy is required, the use of beyond-Voigt line shapes such as the Hartmann–Tran model [24] is necessary.

The detection of $H^{16}OD$ absorption features demonstrate the sensitivity of the spectrometer, despite its low natural abundance (~3.1×10^{-4}). An estimate of the detection sensitivity is obtained from the fit residuals displayed in the inset of Figure 6. Specifically, the minimum detectable absorption coefficient, αmin, that can be determined from the root mean square (rms) of the residuals is equal to 5×10^{-12} cm^{-1}. Under the measurement conditions described, this corresponds to a limit of detection (LOD) for $H^{16}OD$ of approximately 530 ppt. The retrieved αmin value is consistent with that reported by Castrillo et al. [25], for a comparable integration time. In fact, in Ref. [25] the reduction of the LOD, by means of spectral averaging, was clearly demonstrated. αmin decreases with the number of averaged spectra, according to the trend, indicating uncorrelated (Gaussian) noise. For N=2750, corresponding to approximately two days of averaging time, an αmin of $3.7\cdot10^{-13}$ cm^{-1} was achieved.

 doi:10.20944/preprints202604.2096.v1

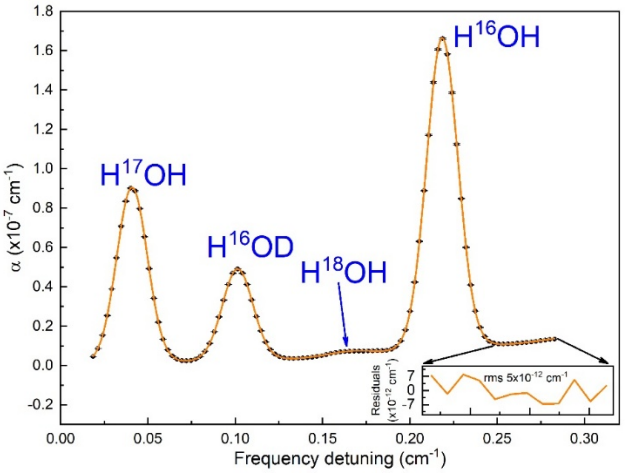

Figure 6. Broadband CRDS absorption spectrum recorded over a frequency span of approximately 9 GHz around 7242 cm⁻¹. The spectrum resolves absorption lines from the four most abundant water isotopologues. The gas sample was extracted from the air of the laboratory and maintained under constant flow conditions into the high-finesse cavity at a pressure of about 3 Torr. Black points represent the experimental data, while the orange curve corresponds to a nonlinear-least squares fit using a sum of Voigt-profiles. The inset panel on the lower part of the figure shows the fit residuals corresponding to the right edge of the spectrum.

4. Validation of the Primary Humidity Generators

4.1. INRIM 03 Mk2 Generator: Validation and Uncertainty

The INRIM trace humidity generator was validated over a frost-point temperature range from −105 °C to −65 °C, corresponding to water vapour amount fractions between 5 nmol·mol⁻¹ and 5 µmol·mol⁻¹, at gas flow rates between 2 L·min⁻¹ and 6 L·min⁻¹, as follows:

- by comparing the reference frost-point temperature, $T_{fp,ref}$, calculated from the measured saturation temperature T_s, saturation pressure p_s, and point-of-use p_c (maintained approximately constant at 1150 hPa), against the frost-point temperature measured by a chilled-mirror hygrometer (PI/MBW SLX);
- by comparing the reference water vapour amount fraction, $x_{w,ref}$, calculated from T_s and p_s, against the amount fraction as measured by CRDS analyser (Photonics Technologies Pure^n-T H_2O).

The validation of the generator was performed by verifying the invariance, within the stated measurement uncertainty, of the difference between the measured and reference values of T_{fp} and x_w while varying pairs of input parameters (T_s, p_s) selected to produce the same nominal frost-point temperature or amount fraction. This approach ensures that the validation remains independent of the (unknown) calibration curve of the comparison instruments. Furthermore, for gas flow rates higher than 2 L·min⁻¹, the saturation efficiency of the generator was evaluated at constant T_{fp} (and constant x_w).

The differences between the measured and reference frost-point temperatures, evaluated as a function of the saturation pressure p_s for N_2 as carrier gas at a nominal frost-point temperature of −100 °C, remain within the uncertainty bars ($k = 1$), which encompass both the uncertainty of the reference frost-point temperature and the resolution and repeatability of the CMH. Minor pressure-dependent trends are observed but are not statistically significant relative to the associated measurement uncertainties. The same validation procedure was applied across the range from −65 °C to −105 °C. The results confirm that the generator delivers a trace humid gas at the designated frost-point temperature when operating in 1T–2P mode for saturation pressures up to 0.65 MPa. The agreement

 doi:10.20944/preprints202604.2096.v1

between measurements at various flow rates confirms saturation efficiency across the 2 L·min^{-1} to 6 L·min^{-1} range.

The relative percent differences between the water vapour amount fraction measured by the CRDS analyser and the corresponding reference value are presented in Figures 7 and 8 as a function of the nominal frost-point temperature (or amount fraction) for N_2 and Ar as carrier gases. Measurements carried out at the minimum and maximum saturation pressures (at a constant flow rate of 2 L·min^{-1}) demonstrate agreement within their uncertainties for both gas mixtures. This confirms that the generator reliably delivers a humid gas with a known water vapour amount fraction for saturation pressures up to 0.65 MPa. However, definitive conclusions could not be drawn at T_{fp} = −105 °C (x_w ≈ 4 nmol·mol^{-1}) due to a lack of available measurements at lower saturation pressures.

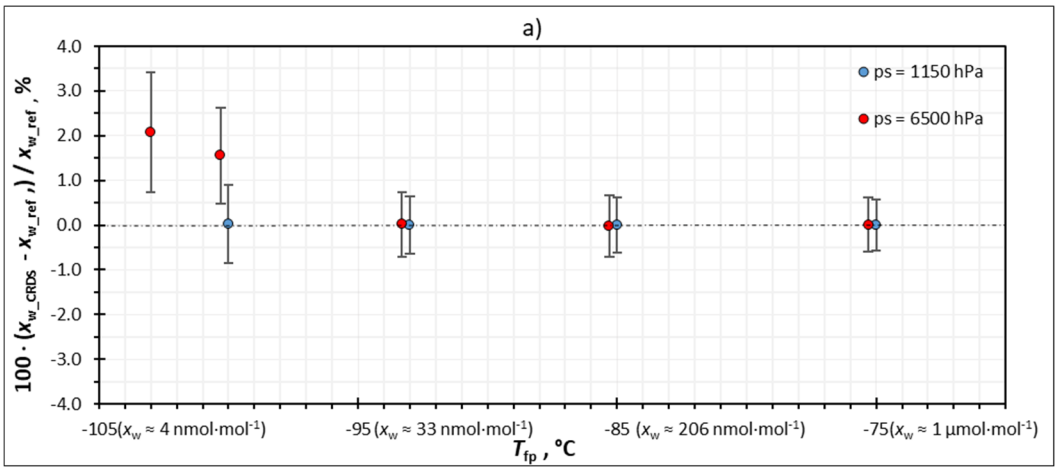

Figure 7. Relative percentage difference between the water vapour amount fraction measured by the CRDS analyser and the reference value for humid N_2-H_2O gas mixture. The plotted results correspond to p_s = 0.65MPa and p_c = 0.115 MPa at each nominal frost-point temperature (and water vapour amount fraction at atmospheric pressure), at a constant flow rate of $\dot{V}$ = 2 l·min^{-1}.

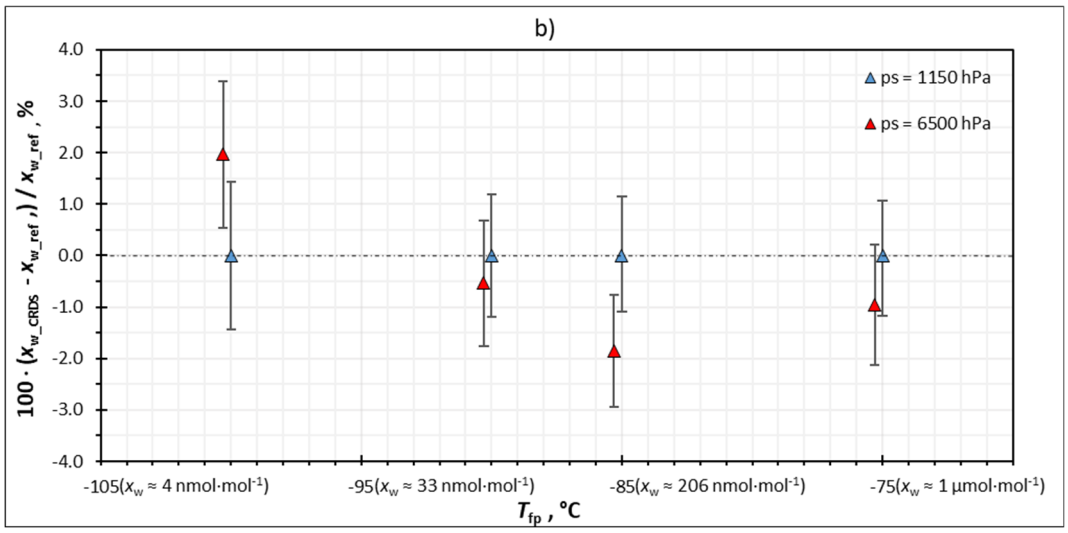

Figure 8. Relative percentage difference between the water vapour amount fraction measured by the CRDS analyser and the reference value for humid Ar-H_2O gas mixture. The plotted results correspond to p_s = 0.65 MPa and p_c = 0.115 MPa at each nominal frost-point temperature (and water vapour amount fraction at atmospheric pressure), at a constant flow rate of $\dot{V}$ = 2 l·min^{-1}.

An exemplary uncertainty budget for the reference frost-point temperature and water vapour amount fraction of the generated gas ($T_{fp,ref}$ and $x_{w,ref}$) is provided for a thermodynamic state defined by p_s = 0.65 MPa, T_s = −97 °C and p_c = 0.115 MPa, which corresponds to nominal T_{fp} = −105 °C and x_w

 doi:10.20944/preprints202604.2096.v1

= 4 nmol·mol^{-1}. This uncertainty budget is presented independently of the specific gas mixture (N_2–H_2O or Ar–H_2O). The enhancement factor was estimated using the Greenspan moist-air formulation [30]; for Ar matrices, this approximation may underestimate the enhancement factor uncertainty by up to 0.2% at high saturation pressures, as the H_2O–Ar cross-virial coefficient differs measurably from the H_2O–air value. Incorporation of gas-matrix-specific enhancement factors [34] is identified as a priority for future refinement of this budget. The main contribution to the combined standard uncertainty arises from the uncertainty in the saturation temperature Ts, whereas the enhancement factor on the saturation side $f(T_s,p_s)$ contributes marginally to the overall budget $u_c(T_{fp,ref})$. Pressure uncertainties were estimated by combining stability, resolution, accuracy and calibration uncertainty of the pressure transducers.

Table 2. Uncertainty budget for the water vapour amount fraction and the frost-point temperature of the generated humid gas evaluated at p_s = 0.65 MPa, T_s = -97 °C and p_c = 0.115 MPa corresponding to a nominal amount fraction of 4 nmol·mol^{-1} and a nominal frost-point temperature of -105 °C.

T_{fp} = -105 °C, p_s = 6500 hPa, T_s = -97 °C, p_c = 1150 hPa, x_w = 4 nmol·mol^{-1}					
Uncertainty budget for $x_{w,ref}$ / mol·mol^{-1}					
Source of uncertainty	Standard uncertainty	PDF	Sensitivity Coefficient	PDF coefficient	Contribution to Standard uncertainty/ mol·mol^{-1}
Saturation pure water vapour pressure, $e(T_s)$	0.0000070 Pa	Normal	1.65·10^{-6}	1	1.15·10^{-11}
Enhancement factor on saturation side, $f(T_s,p_s)$	0.0048	Normal	3.90·10^{-9}	1	1.89·10^{-11}
Saturation temperature, T_s	0.069 °C	Normal	7.98·10^{-10}	1	5.51·10^{-11}
Saturation pressure, p_s	48.4 Pa	Normal	6.41·10^{-15}	1	3.10·10^{-13}
Combined standard uncertainty, $u_c(x_{w,ref})$ / mol·mol^{-1}					5.94·10^{-11}
Combined standard uncertainty, $u_c(x_{w,ref})$ / pmol·mol^{-1}					59
Uncertainty budget for $T_{fp,ref}$ / °C					
Source of uncertainty	Standard uncertainty	PDF	Sensitivity Coefficient	PDF coefficient	Contribution to Standard uncertainty/ °C

 doi:10.20944/preprints202604.2096.v1

Saturation temperature, T_s	0.069 °C	Normal	$8.84 \cdot 10^{-1}$	1	$6.10 \cdot 10^{-2}$
Saturation pressure, p_s	48.4 Pa	Normal	$6.71 \cdot 10^{-6}$	1	$3.25 \cdot 10^{-4}$
Saturation pure water vapour pressure, $e(T_s)$	0.0000070 Pa	Normal	$1.84 \cdot 10^{3}$	1	$1.28 \cdot 10^{-2}$
Enhancement factor on saturation side, $f(T_s,p_s)$	0.0048	Normal	4.32	1	$2.09 \cdot 10^{-2}$
Point-of-use pressure, p_c	85.7 Pa	Normal	$3.95 \cdot 10^{-5}$	1	$3.38 \cdot 10^{-3}$
Enhancement factor at the point-of-use, $f(T_{fp},p_c)$	0.00082	Normal	4.56	1	$3.72 \cdot 10^{-3}$
Combined standard uncertainty, $u_c(T_{fp,ref})$ / °C					0.070

Over the investigated frost-point temperature and water vapour mole fraction ranges, the combined standard uncertainty of $T_{fp,ref}$ varies from 0.03 °C for T_{fp}= −65 °C to 0.07 °C at T_{fp}=−105 °C, while the combined standard relative uncertainty of $x_{w,ref}$ ranges from 0.4 % at x_w = 5 µmol·mol^{-1} to 1.5 % at x_w=4 nmol·mol^{-1}.

4.2. UL FE Generator: Validation and Uncertainty

The upgraded frost-point generator was evaluated over a range from −90 °C frost point to +20 °C dew point and pressures from atmospheric to 1 MPa. This corresponds to the enhancement-factor experiments of the PROMETH2O project. A key limitation was the performance of the chilled-mirror hygrometer below −80 °C, where a strong dependence on flow and water diffusion through the O-ring seal around the mirror was observed. To address this, experiments were designed to separate the hygrometer flow dependence from the saturator efficiency, and the instrument head was modified to mitigate diffusion through the O-ring.

The reference value depends on several system components, including the dew/frost-point CMH (MBW 373LX), SPRT (Accumac), resistance bridge (Batemika UT-ONE B03A), and pressure gauge (Druck PACE1000), whose uncertainties were included in the overall uncertainty budget. In addition, the saturator performance with its temperature stability, temperature uniformity, pressure stability, and saturation efficiency significantly contributes to the total uncertainty.

The stability of the saturator temperature was determined from repeated measurements of the liquid-bath temperature, with the maximum standard deviation taken as the stability contribution. Temperature uniformity was evaluated by measurements at multiple positions inside the bath, including two vertical levels and four circumferential points around the saturator.

Saturation efficiency was assessed by varying the gas flow between 0.2 l·min^{-1} and 3 l·min^{-1}. Pressure stability in the saturator and at the outlet was derived from repeated pressure measurements, while the pressure drop was calculated as the difference between the saturator pressure and the pressure measured at the output sensor.

The resulting uncertainties for dew-point temperatures between −90 °C and +20 °C are summarised in Table 3.

 doi:10.20944/preprints202604.2096.v1

Table 3. Uncertainty budget at different dew/frost point temperatures over the UL FE generator operating range.

Dew/frost-point temperature / °C	-90	-80	-60	-30	+20
Expanded uncertainty (k=2) / °C	0.130	0.068	0.047	0.039	0.038

4.3. VTT Generator: Validation and Uncertainty

The performance of the VTT Low Frost Point Humidity Generator (LFPHG) was validated over its extended operating range with particular focus on ultra-trace humidity levels and elevated pressures. To assess potential incomplete saturation or adsorption effects, a dedicated flow-rate study was performed. The relative deviation of the measured mole fraction from the mean value of the repeatability experiment is illustrated in Figure 9 as a function of flow rate.

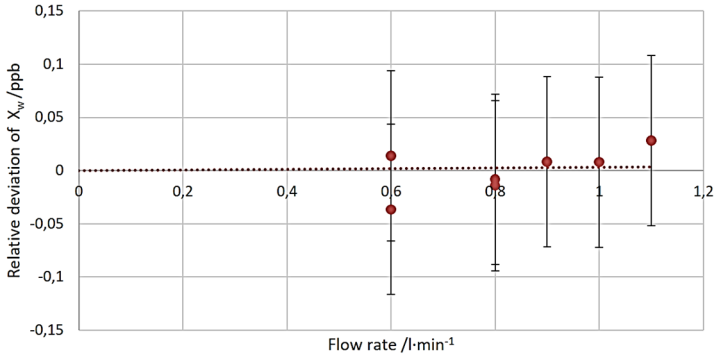

Figure 9. Flow dependence on the condenser, where the relative deviation is calculated as the difference between the water vapour mole fraction at each flow rate and the averaged value of the repeatability experiment.

Within the investigated range (0.6 to 1.1) l·min^{-1}, no statistically significant systematic flow dependence is observed, as indicated by the trend line passing through the origin, where the deviation is expected to approach zero at infinitesimal flow rates. The deviations remain well within the uncertainty limits, confirming adequate residence time in the saturator and negligible flow-induced bias at the operating flow of 0.7 L·min^{-1} used for low frost-point realization. These results support the assumption of sufficiently established thermodynamic equilibrium in the saturator under the selected operating conditions, within the claimed uncertainty levels.

Figure 10 shows the difference between the generated reference amount fraction and the value measured by a CRDS analyser, expressed as Δx_w, as a function of generated amount fraction (Figure 10a) and saturation pressure (Figure 10b).

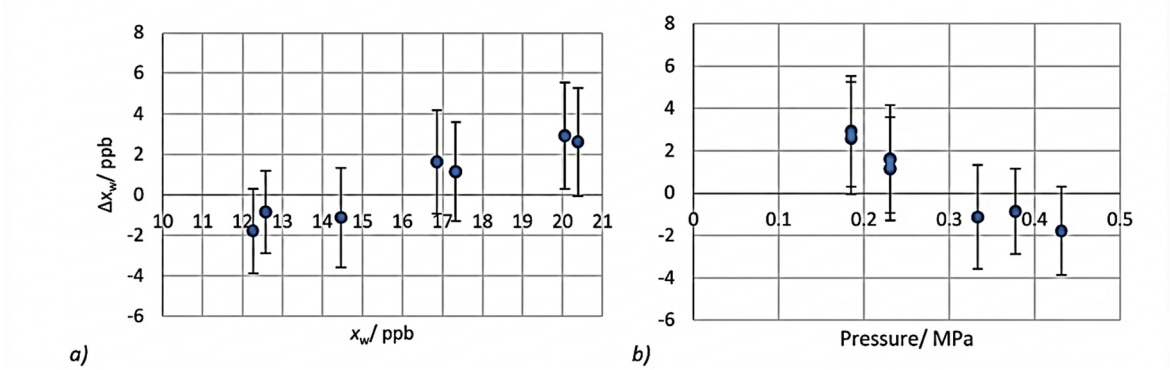

Figure 10. Comparison (difference Δx_w) between the generated reference water vapour amount and the value measured by a CRDS for: (a) a range of generated water vapour amount fraction and (b) at several saturator pressures. Both plots show on the vertical axis the difference Δx_w.

 doi:10.20944/preprints202604.2096.v1

Across the investigated range, the deviations remain within the calculated expanded uncertainties. No significant systematic trend with mole fraction is observed in the trace range, and pressure dependence remains consistent with the thermodynamic model. The results confirm the validity of the 1T-2P realization, and the proper implementation of the saturation equations introduced in Section 3.1.

The frost-point temperature uncertainty was evaluated using the analytical uncertainty model [43]. An example of the frost point temperature uncertainty budget at -100.1 °C is shown in Table 4. The water vapour saturation pressure and its uncertainty are based on the 2011 IAPWS 2011 formulation [44]. The calculation of the water vapour enhancement factor is also based on Hardy's equation [31] and its corresponding uncertainty derived from Lovell-Smith's work [45].

Table 4. Example of uncertainty budget for frost-point temperature at T_{fp} = -100.1 °C.

Source of uncertainty	Standard uncertainty	PDF	Sensitivity Coefficient	PDF coefficient	Contribution to Standard uncertainty/ °C
Saturation temperature stability, T_{sat}	0.0020	Normal	1	1	$2.0 \cdot 10^{-3}$
Saturation temperature uniformity, T_{bath}	0.0083	Rectangular	1	0.289	$2.40 \cdot 10^{-3}$
Calibration uncertainty of the thermometer	0.02	Normal	1	1	$2.0 \cdot 10^{-2}$
Resolution of thermometer	0.0010	Rectangular	1	0.289	$3.0 \cdot 10^{-4}$
SPRT drift	0.001	Rectangular	1	0.289	$8.70 \cdot 10^{-4}$
Self-heating SPRT	0.0007	Rectangular	1	0.289	$2.23 \cdot 10^{-3}$
Adsorption/desorption	0.046	Asy.rectangular	1	0.236	$2.56 \cdot 10^{-2}$
Saturation efficiency	0.015	Rectangular	1	0.289	$4.31 \cdot 10^{-3}$
Combined standard uncertainty, $u_c(T_{fp})$ /°C					0.034

The uncertainty structure confirms that adsorption/desorption and efficiency corrections dominate at ultra-low frost-point temperatures, while pressure-related terms become more relevant at elevated saturation pressures.

5. Discussion and conclusions

5.1. Measurement Uncertainty and Metrological Traceability

The primary humidity systems described in this work represent complementary metrological approaches to trace water measurement in UHP process gases. All three thermodynamic generators (INRIM, UL FE, VTT) established metrological traceability to the SI through calibrated temperature and pressure measurements, combined with the IAPWS formulation for the saturation vapour pressure of ice [44] and the enhancement factor formulations of Greenspan [30], Hardy [31], and Lovell-Smith [45]. For the PTB coulometric generator, traceability is routed through electrical current (the ampere) via Faraday's law [40,41].

 doi:10.20944/preprints202604.2096.v1

The expanded uncertainty (k=2) achieved across the thermodynamic generators at frost-point temperatures between -90 °C and -105 °C is consistently below 0.15 °C. These values are competitive with or superior to the best published results from comparable thermodynamic generators [29,32,38,39] and are consistent with the performance requirements of measurement traceability for trace humidity sensors and analysers in the process gas industry.

INRIM and VTT showed that adsorption and desorption effects dominate at very-low frost points, where the low vapour density means that even sub-monolayer surface coverage can shift the delivered amount fraction measurably. This means that any significant improvements would require advances in surface treatment or flow regime control. INRIM reported the expanded uncertainty at lowest frost point temperature ($U(k=2)$ = 0.13 °C at -105 °C) with the system operating in 1T-2P mode, while VTT reported the expanded uncertainty at -100 °C while operating in 1T-1P mode. The UL FE uncertainty at –90 °C ($U(k=2)$ = 0.13 °C) reflects the combined contributions of dew/frost-point CMH performance degradation below –80 °C and the modified O-ring sealing mitigation strategy described in Section 4.2.

A systematic uncertainty that is not fully accounted for in the current budgets for the N_2 and Ar matrices is the departure of the enhancement factor from the moist-air formulation. For the H_2O–N_2 system at –97 °C and 6500 hPa, Harvey and Huang's ab initio values [46] yield an enhancement factor approximately 0.05 % lower than the Greenspan formulation. For the H_2O–Ar system, the departure reaches 0.15 % to 0.25 % at similar conditions due to the larger second cross-virial coefficient $B_{(H_2O\text{-}Ar)}$. These are comparable in magnitude to the stated relative standard uncertainty of x_w (1.5 % at 4 nmol·mol^{-1}) and should be incorporated into the uncertainty budget as an additional, partially correlated component in future refinements.

5.2. Operational Range and Gas Matrix Compatibility

The four generators together span a frost-point temperature range from –105 °C (~4 nmol mol^{-1}) to +20 °C (~23 mmol·mol^{-1}), covering the full operational envelope of UHP process gas qualification from sub-ppb moisture monitoring up to bulk gas characterisation. The generators have been validated in N_2, CDA, and Ar matrices. Validation in H_2 matrices, which are increasingly critical in the context of hydrogen fuel cell purity specifications (ISO 14687:2019, $x_w \leq 5$ µmol mol^{-1} [47]), remains a priority for future work. The nature of H_2 introduces additional issues for saturator materials and for the enhancement factor formulation, but the PROMETH2O infrastructure provides a validated starting point for such extension.

The CRDS-OFCS spectrometer developed at the University of Campania represents an independent, primary spectroscopic methodology for the determination of water vapour amount fraction measurement that does not rely on thermodynamic saturation. Its demonstrated LOD of ~530 ppt for $H^{16}OD$ with an integration time of about 3.5 hours (equivalent to a main isotopologue $H_2{}^{16}O$ LOD of approximately 100 ppt given the natural $H^{16}OD$:H_2O ratio of ~3.1×10^{-4}) surpasses the detection capabilities of all commercial CRDS analysers cited in the literature. Moreover, its absolute frequency traceability by exploiting an optical frequency comb synthesiser [23,25] makes the CRDS-OFCS a potential primary spectroscopic standard. Future work should establish a comparison between the CRDS-OFCS and the thermodynamic generator, which would constitute the first such comparison in Europe at the sub-ppb level.

5.3. Validation of the Systems and Present Limitations

The validation approach adopted in this work - confirming the invariance of the difference between a thermodynamic generator's reference value and a comparison instrument's indication over a range of input parameter combinations - is independent of the comparison instrument's absolute calibration. This methodology, applied consistently by INRIM (Section 4.1) and VTT (Section 4.3), establishes the internal consistency of each generator over its specified operating range. The agreement between CMH and CRDS analyser indications and INRIM reference values (Figures 7 and 8) and between CRDS analyser and VTT reference values within the stated expanded uncertainties

 doi:10.20944/preprints202604.2096.v1

validates the saturation equation implementation of both systems at the level of the comparison instruments' performance.

An inter-laboratory comparison using a suitable transfer standard would be the next logical step to establish a traceability network at the European level. Until such exercises are available, the goal of European-wide consistency remains provisional.

5.4. Conclusions and Future Directions

This paper has described the development, characterisation, and validation of four complementary primary and reference trace humidity generators - three thermodynamic (1T-2P) and one coulometric - operating in the range from 5 nmol·mol^{-1} to 5 µmol·mol^{-1} in N_2, CDA, and Ar matrices.

The expanded uncertainty (k=2) achieved across the three thermodynamic generators at frost-point temperatures between -90 °C and -105 °C is consistently below 0.15 °C, extending previous capabilities [29,39]. The CRDS-OFCS spectrometer provides an independent, SI-traceable spectroscopic determination of x_w with LOD ~100 ppt (with an integration time of about 3.5 hours), establishing a capability not previously demonstrated in a metrology context.

The validation of PTB's coulometric generator (Section 3.2) over the full scope of operation is currently ongoing as part of a consecutive process. For the range investigated, internal comparisons confirm agreement with a traceable CMH. However, a rigorous uncertainty budget and report of the completed validation process of PTB's system will be reported in a separate publication.

Future work priorities arising from this programme are: (1) inter-laboratory comparison of the four generators using a suitable stable transfer standard; (2) integration of ab initio enhancement factors [46] for N_2 and Ar matrices into the generator uncertainty budgets; (3) extension of validation to H_2 matrix in view of hydrogen fuel cell application requirements.

Nomenclature

AOM	Acoustic-optic modulator
B	Second cross-virial coefficient, cm^3·mol^{-1}
BOA	Booster-optical-amplifier
c	Vacuum speed of light, m·s^{-1}
CDA	Clean Dry Air
CMH	Chilled-Mirror Hygrometer
CRDS	Cavity Ring-Down Spectroscopy
CTHG	Coulometric trace-humidity generator
DUC	Device under calibration
e_s	Saturation water vapour pressure, Pa
F	Faraday constant, C mol^{-1}
FTIR	Fourier Transform Infrared
f	Enhancement factor, dimensionless
GC	Gas Chromatography
GUM	Guide to the Expression of Uncertainty in Measurement
HBr	Hydrogen bromide
HCl	Hydrogen Chloride
H_2	Hydrogen
I	Electric current, A
IAPWS	International Association for the Properties of Water and Steam
k	Expanded uncertainty, °C

 doi:10.20944/preprints202604.2096.v1

k_B	Boltzmann constant, J·K^{-1}
LFPHG	Low Frost Point Humidity Generator
LOD	Limit of detection
M_{N_2}	Molar mass of nitrogen, g mol^{-1}
M_w	Molar mass of water vapour, $g\ mol^{-1}$
m_{N_2}	Mass of nitrogen, g
m_w	Mass of water vapour, g
$\dot{m}_{N_2}$	Mass flow rate of nitrogen, kg s^{-1}
$\dot{m}_w$	Mass flow rate of water vapour, $kg\ s^{-1}$
MFC	Mass-flow controller
MS	Mass Spectrometry
N	Comb tooth order
n	Amount of water molecules, mol
NH_3	Ammonia
N_2	Nitrogen
NMI	National Metrology Institute
O_2	Oxygen
P	Pressure gauge
p	Gas pressure, Pa
p_s	Saturation pressure, Pa
p_c	Point-of-use pressure, Pa
PDF	probability density function
PHD	Pound-Drever-Hall
PID	Proportional–Integral–Derivative
PL	Probe Laser
ppb	part per billion
ppm	part per million
PRT	Platinum resistance thermometer
Q	Electric charge, C
r	Mixing ratio, dimensionless
rms	Root mean square
RH	Relative humidity
RL	Reference oscillator
Rh	Rhodium
SI	International System of Units
$S(T)$	Temperature-dependent line intensity, cm·molecule^{-1}
SPRT	Standard platinum resistance thermometer
t	Time, s
TEC	Thermoelectric cooler
TDLAS	Tuneable Diode Laser Absorption Spectroscopy
OFCS	Optical Frequency Comb Synthesiser
T	Thermodynamic temperature, K
T_{fp}	Frost-Point Temperature, °C
$T_{fp,ref}$	Reference Frost-Point Temperature, °C

 doi:10.20944/preprints202604.2096.v1

T_s	Saturation temperature, °C
u_c	Combined standard uncertainty, mol·mol^{-1}
U_c	Expanded uncertainty, K
UHP	Ultra-High Purity
V_0	Molar volume of the ideal gas, m^3 mol^{-1}
V	Volume, m^3
$\dot{V}$	Flow rate at standard conditions, l min^{-1}
V	Valve
x_{ref}	Reference water vapour amount fraction, nmol mol^{-1}
x_w	Water vapour amount fraction, nmol mol^{-1}
z	Number of transferred electrons, dimensionless

Greek symbols

α_{min}	Minimum detectable absorption coefficient, cm^{-1}
α_{TOT}	Integrated absorption coefficient, cm^{-1}
ν	Frequency, Hz
τ	Decay time, s
τ_0	Empty-cavity decay constant, s

Acknowledgments: This work has been carried out within the European Metrology Programme for Innovation and Research (EMPIR) Project "PROMETH2O - Metrology for trace water in ultra-pure process gases". This project (Grant No. 20IND06 PROMETH2O) has received funding from the EMPIR programme co-financed by the Participating States and from the European Union's Horizon 2020 research and innovation programme.

AI Statement: The authors acknowledge the use of AI tools exclusively to improve the English language quality of the manuscript and to support manuscript editing to check the consistency of symbol quantities throughout the manuscript and the nomenclature table. No content interpretation or data analysis was carried out using AI tools.

References

1. Funke, H.H.; Grissom, B.L.; McGrew, C.E.; Raynor, M.W. Techniques for the measurement of trace moisture in high-purity electronic specialty gases. Rev. Sci. Instrum. 2003, 74, 3909–3933. DOI: 10.1063/1.1597939.
2. Bell, S.; Gardiner, T.; Stevens, M.; Waterfield, K. Evaluation of Trace Moisture Sensors – Interim Report; National Physical Laboratory Report CBTLM 19; NPL & BOC Edwards: Teddington, UK, 2002.
3. Bell, S.; Gardiner, T.; Gee, R.; Stevens, M.; Waterfield, K.; Woolley, A. An Evaluation of Performance of Trace Moisture Measurement Methods; National Physical Laboratory Report; NPL: Teddington, UK, 2004.
4. Raynor, M.W.; Bertness, K.A.; Cossel, K.C.; Adler, F.; Ye, J. Trace Water Vapor Analysis in Specialty Gases: Sensor and Spectroscopic Approaches. In Trace Analysis of Specialty and Electronic Gases; Geiger, W.M., Raynor, M.W., Eds.; Wiley: Hoboken, NJ, USA, 2013; pp. 195–249.
5. Margolis, S.A.; Huang, P.H.; Hadaruga, N.G.; Hadaruga, D.I. Water Determination. In Encyclopedia of Analytical Science, 3rd ed.; Elsevier: Amsterdam, The Netherlands, 2019; pp. 382–390. DOI: 10.1016/B978-0-12-409547-2.14505-6.
6. Nie, J.; Liu, X. A review of dew point sensors: Recent advances and future development. Sens. Actuators B Chem. 2024, 417, 136115. DOI: 10.1016/j.snb.2024.136115.
7. Poltera, Y., Belmonte, A., Luo, B. P., Jorge, T. R., Vömel, H., Wienhold, F. G., & Peter, T. The "Golden Points" of the Cryogenic Frost Point Hygrometer: a new method to reduce measurement noise and improve the precision of stratospheric water vapor measurements. Atmospheric Measurement Techniques, 14(11), 7231–7246 (2021).

 doi:10.20944/preprints202604.2096.v1

8. Takeda, N.; Carroll, P.; Tsukahara, Y.; Beardmore, S.; Bell, S.; Yamanaka, K.; Akao, S. Trace moisture measurement in natural gas mixtures with a single calibration for nitrogen background gas. Meas. Sci. Technol. 2020, 31, 104007. DOI: 10.1088/1361-6501/ab94ff.
9. Tao, J.; Luo, Y.; Wang, L.; Cai, H.; Sun, T.; Song, J.; Liu, H.; Gu, Y. An ultrahigh-accuracy miniature dew point sensor based on an integrated photonics platform. Sci. Rep. 2016, 6, 29672. DOI: 10.1038/srep29672.
10. Rosenthal, P.; Spartz, M.L. Instrumentation for real-time trace impurity detection of bulk ammonia in production environments. Gases Technol. 2003, 25, 8–12.
11. Stallard, B.R.; Rowe, R.K.; Garcia, M.J.; Haaland, D.M.; Espinoza, L.H.; Niemczyk, T.M. Trace Water Vapor Determination in Corrosive Gases by Infrared Spectroscopy; Sandia National Laboratories Report SAND 93-4026 UC-411; SNL: Albuquerque, NM, USA, 1993.
12. Cui, X.; Dong, F.; Zhang, Z.; Xia, H.; Pang, T.; Sun, P.; Wu, B.; Liu, S.; Han, L.; Li, Z.; Yu, R. Environmental application of high sensitive gas sensors with tunable diode laser absorption spectroscopy. In Green Electronics; Donchev, V., Ed.; IntechOpen: Rijeka, Croatia, 2018. DOI: 10.5772/intechopen.76448.
13. Werle, P. Accuracy and precision of laser spectrometers for trace gas sensing in the presence of optical fringes and atmospheric turbulence. Appl. Phys. B 2011, 102, 313–329. DOI: 10.1007/s00340-010-4165-9.
14. Nelson, D.D.; Shorter, J.H.; McManus, J.B.; Zahniser, M.S. Sub-part-per-billion detection of nitric oxide in air using a thermoelectrically cooled mid-infrared quantum cascade laser spectrometer. Appl. Phys. B 2002, 75, 343–350. DOI: 10.1007/s00340-002-0979-4.
15. Funke, H.H.; Yao, J.; Raynor, M.W.; Wright, A.O. Using tunable diode laser spectroscopy to detect trace moisture in ammonia. Solid State Technol. 2004, 47, 49–54.
16. McAndrew, J.; Bartolomey, M.; Girard, J.M.; Goltz, G.; Han, J.M. Implementing on-line and in-situ moisture monitoring in reactive gas environments. Micro 2000, 18, 39–47.
17. B. Buchholz, N. Böse, and V. Ebert, Absolute validation of a diode laser hygrometer via intercomparison with the German national primary water vapor standard. Appl. Phys. B 2014, 116, 883–899, doi: 10.1007/s00340-014-5775-4.
18. 18.J. Nwaboh, S. Pratzler, and V. Ebert "First metrological validation of TwOGaSt, a new, absolute dTDLAS-trace-hygrometer, using the primary, coulometric, trace water vapour generator at PTB" tm - Technisches Messen, vol. 90, no. 1, 2023, pp. 57-64. https://doi.org/10.1515/teme-2022-0024
19. Mazurenka, M.; Orr-Ewing, A.J.; Peverall, R.; Ritchie, G.A.D. Cavity ring-down and cavity enhanced spectroscopy using diode lasers. Annu. Rep. Prog. Chem., Sect. C 2005, 101, 100–142. DOI: 10.1039/B408909J.
20. O'Keefe, A.; Deacon, D.A.G. Cavity ring-down optical spectrometer for absorption measurements using pulsed laser sources. Rev. Sci. Instrum. 1988, 59, 2544–2551. DOI: 10.1063/1.1139895.
21. Dudek, J.B.; Tarsa, P.B.; Velasquez, A.; Wladyslawski, M.; Rabinowitz, P.; Lehmann, K.K. Trace moisture detection using continuous-wave cavity ring-down spectroscopy. Anal. Chem. 2003, 75, 4599–4605. DOI: 10.1021/ac0343073.
22. Abe, H.; Yamada, K.M.T. Performance evaluation of a trace-moisture analyzer based on cavity ring-down spectroscopy: Direct comparison with the NMIJ trace-moisture standard. Sens. Actuators A Phys. 2011, 165, 230–238. DOI: 10.1016/j.sna.2010.11.005.
23. Gianfrani, L.; Hu, S.-M.; Ubachs, W. Advances in cavity-enhanced methods for high precision molecular spectroscopy and test of fundamental physics. Riv. Nuovo Cimento 2024, 47, 229–298. DOI: 10.1007/s40766-024-00051-4.
24. Gordon, I.E.; Rothman, L.S.; Hargreaves, R.J.; Hashemi, R.; Karlovets, E.V.; Skinner, F.M.; Conway, E.K.; Hill, C.; Kochanov, R.V.; Tan, Y.; et al. The HITRAN2020 molecular spectroscopic database. J. Quant. Spectrosc. Radiat. Transf. 2022, 277, 107949. DOI: 10.1016/j.jqsrt.2021.107949.
25. Castrillo, A.; Khan, M.A.; Fasci, E.; D'Agostino, V.; Gravina, S.; Gianfrani, L. Demonstration of record sensitivity for water vapour detection by means of comb-locked cavity ring-down spectroscopy. Optica 2024, 11, 1277–1284. DOI: 10.1364/OPTICA.524831.
26. Kassi, S.; Campargue, A. Cavity ring down spectroscopy with 5×10^{-13} cm^{-1} sensitivity. J. Chem. Phys. 2012, 137, 234201. DOI: 10.1063/1.4769974.

 doi:10.20944/preprints202604.2096.v1

27. Fasci, E.; D'Agostino, V.; Khan, M.A.; Gravina, S.; Porzio, G.; Gianfrani, L.; Castrillo, A. Comb-assisted cavity ring-down spectroscopy for ultra-sensitive traceable measurements of water vapour in ultra-high purity gases. J. Phys.: Conf. Ser. 2023, 2439, 012017. DOI: 10.1088/1742-6596/2439/1/012017.
28. Fasci, E.; Khan, M.A.; D'Agostino, V.; Gravina, S.; Fernicola, V.; Gianfrani, L.; Castrillo, A. Water vapor concentration measurements in high purity gases by means of comb assisted cavity ring down spectroscopy. Sens. Actuators A Phys. 2023, 362, 114632. DOI: 10.1016/j.sna.2023.114632.
29. Cuccaro, R.; Beltramino, G.; Rosso, L.; Nobakht, R.; Fernicola, V. Assessment of the INRIM trace water generator and analysis of the uncertainty components down to −100 °C frost-point temperature. Metrologia 2024, 61, 045003. DOI: 10.1088/1681-7575/ad53cc.
30. Greenspan, L. Functional equations for the enhancement factors for CO_2-free moist air. J. Res. Natl. Bur. Stand. A 1976, 80, 41–44. DOI: 10.6028/jres.080A.007.
31. Hardy, B. ITS-90 formulation for vapor pressure, frost point temperature, dewpoint temperature, and enhancement factors in the range −100 to +100 °C. In Proceedings of the Third International Symposium on Humidity and Moisture, London, UK, 6–8 April 1998; National Physical Laboratory: Teddington, UK, 1998; Vol. 1, pp. 214–222.
32. FitzGerald, C.; Mac Lochlainn, D.; Strnad, R.; Hodžić, N. Development of a new primary humidity measurement standard. Meas. Sci. Technol. 2020, 31, 024003. DOI: 10.1088/1361-6501/ab4c3d.
33. Cuccaro, R.; Rosso, L.; Smorgon, D.; Beltramino, G.; Tabandeh, S.; Fernicola, V. Development of a low frost-point generator operating at sub-atmospheric pressure. Meas. Sci. Technol. 2018, 29, 054006. DOI: 10.1088/1361-6501/aaa785.
34. Radicevic, I.; Hudoklin, D. Empirical enhancement factors for trace moisture in nitrogen and argon: Bridging measurement principles. Sens. Actuators B Chem. 2025, 435, 137617. DOI: 10.1016/j.snb.2025.137617.
35. Fernicola, V.; Arpino, F. Design and modelling of a low frost-point humidity generator. In Proceedings of the Joint International Symposium on Temperature, Humidity, Moisture and Thermal Measurements in Industry and Science (TEMPMEKO/ISHM), Portorož, Slovenia, 31 May–4 June 2010.
36. Hudoklin, D.; Dmovšek, J. The new LMK primary standard for dew-point sensor calibration: Evaluation of the high-range saturator efficiency. Int. J. Thermophys. 2008, 29, 1652–1659. DOI: 10.1007/s10765-007-0367-8.
37. Hudoklin, D.; Jokovski, B.; Nielsen, J.; Dmovšek, J. Design and validation of a new primary standard for calibration of the top-end humidity sensors. Measurement 2008, 41, 950–959. DOI: 10.1016/j.measurement.2008.01.006.
38. Sairanen, H.; Heinonen, M.; Högström, R. Validation of a calibration set-up for radiosondes to fulfil GRUAN requirements. Meas. Sci. Technol. 2015, 26, 105901. DOI: 10.1088/0957-0233/26/10/105901.
39. Sairanen, H.; Heinonen, M.; Högström, R.; Salminen, J.; Saxholm, S.; Kajastie, H. Low-pressure and low-temperature dew/frost-point generator. Int. J. Thermophys. 2018, 39, 104. DOI: 10.1007/s10765-018-2425-9.
40. Mackrodt, P. A new attempt on a coulometric trace humidity generator. Int. J. Thermophys. 2012, 33, 1520–1535. DOI: 10.1007/s10765-012-1348-0.
41. Gliese, P.J.; Bubser, F.; Deschermeier, R. Das coulometrische Prinzip als Grundlage eines Spurenfeuchtegenerators [The coulometric principle as the basis of a trace-moisture generator]. Tech. Mess. 2024, 91, 613–618. DOI: 10.1515/teme-2024-0015.
42. Schröder, V.; Emonts, B.; Janßen, H.; Schulze, H.-P. Explosion limits of hydrogen/oxygen mixtures at initial pressures up to 200 bar. Chem. Eng. Technol. 2004, 27, 847–851.]
43. BIPM; IEC; IFCC; ILAC; ISO; IUPAC; IUPAP; OIML. Evaluation of Measurement Data—Guide to the Expression of Uncertainty in Measurement (GUM); JCGM 100:2008; BIPM: Sèvres, France, 2008. DOI: 10.59161/JCGM100-2008E.
44. Wagner, W.; Riethmann, T.; Feistel, R.; Harvey, A.H. New equations for the sublimation pressure and melting pressure of H_2O ice Ih. J. Phys. Chem. Ref. Data 2011, 40, 043103. DOI: 10.1063/1.3657937.
45. Lovell-Smith, J. An expression for the uncertainty in the water vapour pressure enhancement factor for moist air. Metrologia 2007, 44, L49–L52. DOI: 10.1088/0026-1394/44/6/N02.

 doi:10.20944/preprints202604.2096.v1

46. Harvey, A.H.; Huang, P.H. Second cross-virial coefficients and enhancement factors for water vapour in noble gases, nitrogen, hydrogen, and carbon dioxide. J. Phys. Chem. Ref. Data 2020, 49, 033101. DOI: 10.1063/5.0011094.
47. ISO 14687:2019. Hydrogen Fuel — Product Specification; International Organization for Standardization: Geneva, Switzerland, 2019.
48. SEMI C3 - Specification for Electronic Gases, Semiconductor Equipment and Materials International, 2018.
49. EMPIR project PROMETH2O - Metrology for trace water in ultra-pure process gases (www.prometh2o.eu/).